Available online at www.sciencedirect.com

SciVerse ScienceDirect

Ceramics International 38 (2012) 5069–5080

CERAMICS INTERNATIONAL

www.elsevier.com/locate/ceramint

Dielectric and magnetic study of $BaTi_{0.5}Mn_{0.5}O_3$ ceramics, synthesized by solid state sintering, mechanical alloying and chemical routes

R.N. Bhowmik *

Department of Physics, Pondicherry University, R. Venkataraman Nagar, Kalapet, Pondicherry-605014, India

Received 4 February 2012; received in revised form 3 March 2012; accepted 4 March 2012
Available online 9 March 2012

Abstract

A comparative study of the surface morphology, dielectric and magnetic properties of the $BaTi_{0.5}Mn_{0.5}O_3$ (BTMO) ceramics has been carried out by synthesizing the samples in different routes. BTMO samples have shown single phased 12R type hexagonal structure with $R\bar{3}m$ space group. Interfacial effects on the dielectric properties of the samples have been understood by Cole–Cole plots in complex impedance and modulus formalism. It has been found that huge dielectric constant (10^3–10^6) at lower frequencies is largely contributed by the heterogeneous electronic microstructure at the interfaces of grains. Modulus formalism has identified the effects of both grain and grain boundary microstructure on the dielectric properties, particularly in chemical routed samples. The order of grain boundary resistivity suggests the semiconductor/insulator class of the material. The grain boundary resistivity of the mechanical alloyed samples is remarkably lower than the solid state and chemical routed samples. Some of the samples have exhibited signature of weak ferromagnetism at room temperature.

Keywords: A. Powders: chemical preparation; B. Grain boundaries; C. Dielectric properties; D. Transition metal oxides; E. Functional applications

1. Introduction

Perovskite structured (ABO_3) transitional metal oxides have received tremendous research interest in terms of basic theory, novel phenomena and technological applications [1,2]. Recent studies have focused on the establishment of the connectivity between lattice, spin and electronic structure of many novel perovskites [3–6]. Multi-ferroic perovskite is one of such materials where magnetism and ferroelectric polarization are coexisting in the same crystal structure. The experimental results of electric field controlled magnetism and vice versa [7,8] have opened a new route for developing spintronic materials that can be applied in electronic switches, magnetic sensors and memory devices [9]. $BaTiO_3$ is a widely used ferroelectric material for the fabrication of multilayer capacitors, positive temperature coefficient (PTC) thermistors, piezoelectric transducers, and electro-optic devices [10]. Room temperature dielectric constant of $BaTiO_3$ exhibited in a wide range of 200–7000. It is understood that dielectric properties of $BaTiO_3$ samples are strongly dependent on grain size, heterogeneity in microstructure, domain configuration, and preparation process [11–16]. Hence, microstructure and related parameters have a significant role on ferroelectric properties, although non-centrosymmetricity of Ti^{4+} cations is the root cause for ferroelectricity in $BaTiO_3$ based ceramics [17]. Interestingly, Ti^{4+} cations with an empty d-shell (d^0) at octahedral (B) sites attribute non-magnetic character of $BaTiO_3$ ceramics. Magnetism, in contrast, requires transition metal (TM: Cr^{3+}, Mn^{3+}, Fe^{3+}) ions at the B-sites with partially filled d or f shells. Nakayama and Katayama-Yoshida [18] studied the stability of ferroelectric and magnetic structures of transition metal (M = Sc, V, Cr, Mn, Fe, Co, Ni, Cu) doped $BaTiO_3$. They predicted better ferromagnetism in Cr, Mn, and Fe doped $BaTiO_3$. Among these compounds, Mn doped $BaTiO_3$ appeared to be most promising. Proper amount of Mn^{2+} doping could be effective to reduce the dielectric loss in $BaTiO_3$ [19] and it is useful for applying $BaTiO_3$ based ceramics in microwave devices. Thus, synthesis and study of $Ba(Ti_{1-x}M_x)O_3$ could be interesting for basic understanding and applications point of view. In Mn-doped $BaTiO_3$ film [20], Mn ions were in Mn^{2+} state, along with less amount Mn^{3+} and Mn^{4+} ions. Shuai et al. [21] indicated the presence of Mn^{4+} ions in 5% Mn-doped $BaTiO_3$. Qin et al. [22] showed ferromagnetism in UV-irradiated

* Tel.: +91 9944064547; fax: +91 4132655734.
E-mail address: rnbhowmik.phy@pondiuni.edu.in.

0272-8842/$36.00
doi:10.1016/j.ceramint.2012.03.009

(defect-assisted) $BaTiO_3$ nanoparticles. On the other hand, $BaMnO_3$ is a poor ferroelectric material with dielectric constant ~15 at room temperature. Hence, there is a large scope of manipulating structure, magnetism and dielectric properties in $Ba(Mn,Ti)O_{3-\delta}$ compounds [23].

In this work, we have synthesized the composition $BaMn_{0.5}Ti_{0.5}O_3$. Our aim is to present a comparative study of the structure, grain morphology, dielectric and magnetic properties of the material synthesized by different routes. Some important results of the $BaMn_{0.5}Ti_{0.5}O_3$ ceramics will be highlighted viewing their potential applications in microelectronics.

2. Experimental

2.1. Materials synthesis

The composition $BaMn_{0.5}Ti_{0.5}O_3$ (BTMO) was prepared using three different routes, viz., (1) solid state sintering (SS), (2) mechanical alloying (MA) and subsequent annealing in the temperature range 1273–1473 K, and (3) complex hydroxide mediated (CHM) chemical route. In solid state sintering route, required amounts of high purity $BaCO_3$ (purity > 99.99%), MnO_2 (purity > 99.99%) and TiO_2 (purity > 99.99%) were mixed to obtain the composition $BaTi_{0.5}Mn_{0.5}O_3$. The mixed powder was ground for 2 h using mortar and pestle. This was followed by heating at 1273 K of 24 h to remove the CO_2 from $BaCO_3$. The powder was reground and made into pellets under 5 ton pressure. The pellets were sintered at 1373 K for 24 h and at 1473 K for 6 h with intermediate cooling to room temperature. In mechanical alloying route, required amounts of the powders $BaCO_3$ (purity > 99.99%), MnO_2 (purity > 99.99%) and TiO_2 (purity > 99.99%) were taken into a silicon nitride bowl (45 ml). The mixed powders were added with 10 silicon nitride (10 mm diameter) balls and 7 tungsten carbide (5 mm diameter) balls into a bowl with ball to powder mass ratio at 1:6. FRITSCH planetary mono mill (P-6, Germany) was used for mechanical alloying of the powders in air. The milling was continued at 300 rpm. XRD pattern showed that $BaCO_3$ phase was largely non-reactive in 64 h and also in 88 h milled samples. Previous reports [24,25] showed successful synthesis of $BaTiO_3$ either through direct mechanical alloying or by annealing of the mechanical alloyed powder at higher temperatures. We prepared two pellets from each of the 64 h and 88 h mechanical alloyed powders. We heated the pellets in two batches at 1273 K (A) and at 1473 K (B) separately for 6 h. The heating and cooling rates were maintained at 5 K/min. In CHM route [26], required mixture of $BaCl_2$, MnO_2, and TiO_2 was taken in a BOROCIL beaker. $BaCl_2$ was obtained by reacting $BaCO_3$ with dilute HCl solution. The mixture of 0.27 g NaOH and 0.33 g of KOH was added to the solution inside the beaker for the synthesis of 1 g $BaTi_{0.5}Mn_{0.5}O_3$. The beaker was heated at 573 K. The molten solution was stirred to make homogeneous. The solution was kept at 523 K for 24 h, followed by slow cooling to room temperature to form a solid product. The solid product was collected from the beaker. The solid product was ground and then, added it in distilled water to clean the by-products. The solid powder was then dried and made into pellets. Two pellets were annealed separately at 1273 K and at 1423 K for 6 h with heating and cooling at 5 K/min. The samples in different routes have been coded in Table 1.

Table 1
Code of the samples prepared by different preparation routes.

Sample code	Synthesis procedure
BTMO-bulk	Solid state sintering route with final heating up to 1473 K for 6 h
BTMO-64MA	Mechanical alloying with milling time 64 h
BTMO-88MA	Mechanical alloying with milling time 88 h
BTMO-64A	Pelletizing sample of BTMO-64 that was annealed at 1273 K for 6 h
BTMO- 88A	Pelletizing sample BTMO-88 and annealing at 1273 K for 6 h
BTMO-64B	Pelletizing sample of BTMO-64 that was annealed at 1473 K for 6 h
BTMO- 88B	Pelletizing sample BTMO-88 and annealing at 1473 K for 6 h
BTMO-CP	Chemical precipitation with heating at 523 K for 24 h.
BTMO-CP-A	Pelletizing of sample BTMO-CP and annealing at 1273 K for 6 h
BTMO-CP-B	Pelletizing of sample BTMO-CP and annealing at 1423 K for 6 h

2.2. Material characterization

Crystalline structure of the samples was studied using X-pert PANalytical X-ray diffractometer with CuKα radiation (2θ range: 20–80° with step size 0.02°). Room temperature X-ray diffraction (XRD) profile was fitted using FULLPROF-suite program. Surface morphology of the samples was studied using Scanning Electron Microscope (HITACHI S-3400N). Energy dispersive X-ray (EDX) technique was used to estimate the elemental composition of selected samples. The field (0–15 kOe) dependence of dc magnetization was carried out by VSM (Lakeshore-7404). Dielectric properties of the materials were measured using broadband dielectric spectrometer (Novocontrol Technologies, Germany) at amplitude 1 V with frequencies 1 Hz to 3 MHz. The pellet-shaped samples were sandwiched between two gold-coated plates that were connected to the spectrometer with special cables.

3. Results and discussion

3.1. Microstructure study

Fig. 1 shows the XRD profile fit for selected samples. Table 2 shows the refined cell parameters. XRD pattern of the BTMO samples (Fig. 1(b–f)) is drastically different from the XRD pattern of the $BaTiO_3$ (BTO) sample (Fig. 1(a)). The BTO sample was obtained by heating the pellet form of $BaTiO_3$ powder at 1473 K for 24 h. High purity (99.9%) $BaTiO_3$ powder was procured from Sigma–Aldrich Chemicals. XRD pattern of the BTO sample matched to tetragonal structure with space group P4mm. The lattice parameters (a = 3.9963 Å,

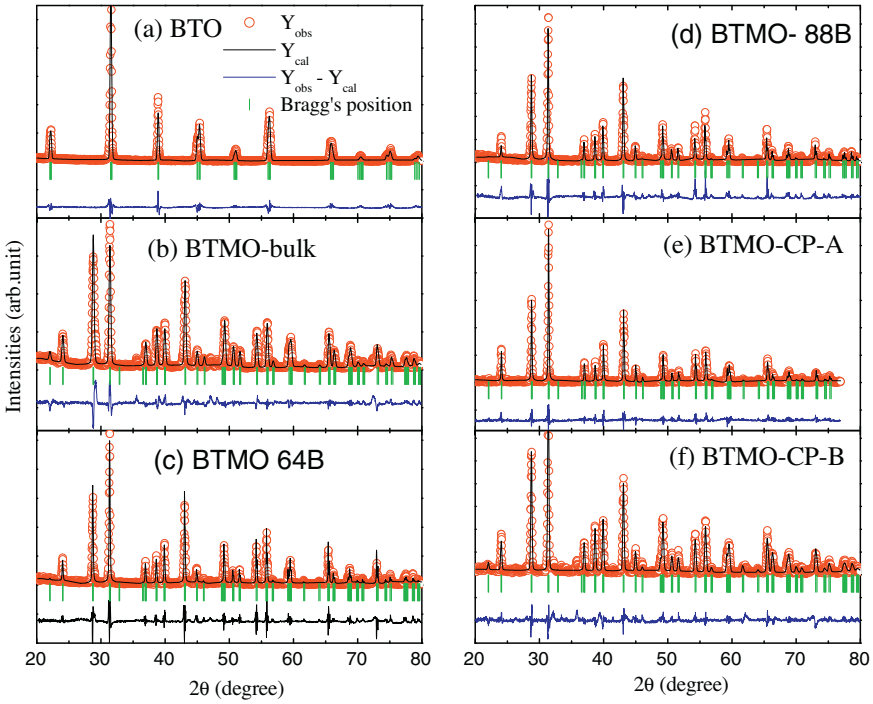

Fig. 1. Experimental and profile fit of room temperature XRD pattern for different samples.

$c = 4.0229$ Å, $V = 64.25$ Å^3) of BTO sample were in good agreement to reported value [25,27]. On the other hand, patterns of BTMO samples are best fitted into 12R type hexagonal structure with space group $R\bar{3}m$ [19,27]. This means the structure of Mn doped BTO samples are stabilized into lower symmetric $BaMnO_3$ type structure. Cell volume has also increased in BTMO samples. Fig. 2(a–d) shows typical surface morphology (SEM) of BTMO-64MA, BTMO-64B, BTMO-88B, and BTMO-CP-B samples. The image of BTMO-64MA sample (Fig. 2(a)) shows more of diffused particles taking nearly spherical shaped with average size 60–80 nm. The particles of the heat-treated BTMO-64B sample (Fig. 2(b)) shaped into rectangular rod/thick plate with length 2–5 μm, width 800 nm to 1.2 μm and thickness 500–800 nm. The plate shape of the particles, also reported by Wu et al. [28], are more clear in BTMO-88B sample (Fig. 2(c)) with length 2–4.5 μm, width 1–1.5 μm and thickness 700–800 nm. The chemical routed BTMO-CP-B sample (Fig. 2(d), on the other hand, showed bimodal distribution with diameter nearly 700–800 nm and 200–400 nm for large and small of particles, respectively. SEM data indicated that surface morphology of the chemical routed sample, where small particles are agglomerated or nucleating over the surfaces of larger particles, are drastically different from the relatively smooth surfaces of mechanical and solid state routed (picture not shown) samples. SEM picture also shows better compactness/connectivity (semi-melt like state) of the particles in chemical routed samples. EDX pattern identified the major elements Ba, Ti, and Mn with ratio 1:0.52:0.48 and 1:0.51:0.48 for BTMO-64B and BTMO-88B, respectively. The atomic ratio of Ba, Ti and Mn is close to the expected value 1:0.5:0.5. The results show that oxygen content per Ba atom is ∼2.82. The oxygen deficiency may be genuine [28] or due to inexact determination of low atomic numbered oxygen atoms from EDX pattern.

3.2. Dielectric properties

3.2.1. Ac conductivity

Fig. 3 shows the frequency (f) dependence of the real part (σ') of ac conductivity at selected temperatures in the range

Table 2
Lattice parameters of the samples from the profile fit of XRD pattern. Activation energy (E_a) and characteristic relaxation time (τ_0) were calculated from the temperature dependence of resistivity ($\rho(T)$ and relaxation time ($\tau_g(T)$) fit to Arrhenius law.

Sample	Lattice parameters			Activation energy (eV) from				τ_{gb0} (10^{-11} s)	τ_{g0} (10^{-12} s)
	a (Å)	c (Å)	V (Å)^3	$\rho_{gb}(T)$ data	$\rho_g(T)$ data	$\tau_{gb}(T)$ data	$\tau_g(T)$ data		
BTMO-bulk	5.6987	27.892	780.49	0.55	–	0.52	0.38	1.0	33985
BTMO-64B	5.7027	27.936	786.79	0.44	–	0.46	0.36	2.4	8.17
BTMO-88B	5.7020	27.944	786.83	0.43	–	0.44	0.38	13.6	1.62
BTMO-CP-A	5.6901	27.916	782.77	–	0.44	–	0.41	–	5.42
BTMO-CP-B	5.6965	27.954	785.61	0.47	–	0.45	–	300	–

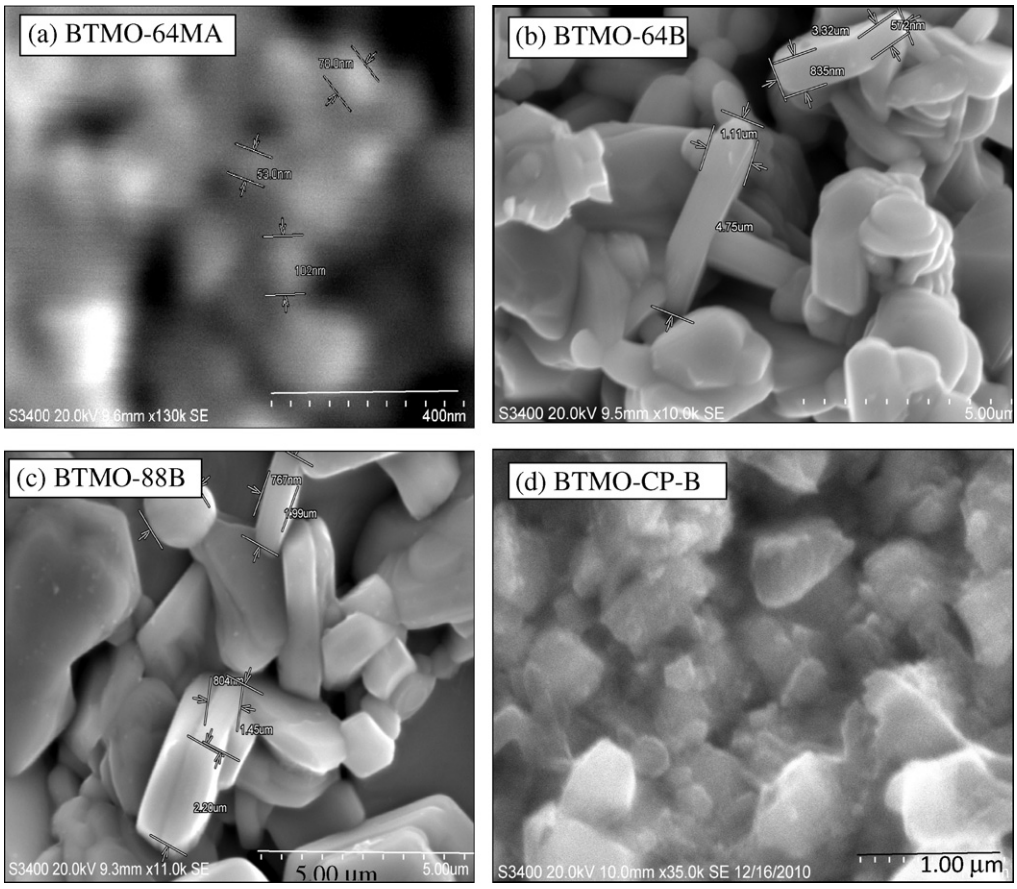

Fig. 2. SEM pictures for the samples BTMO-64MA (a), BTMO-64B (b), BTMO-88B (c) and BTMO-CP-B (d), respectively.

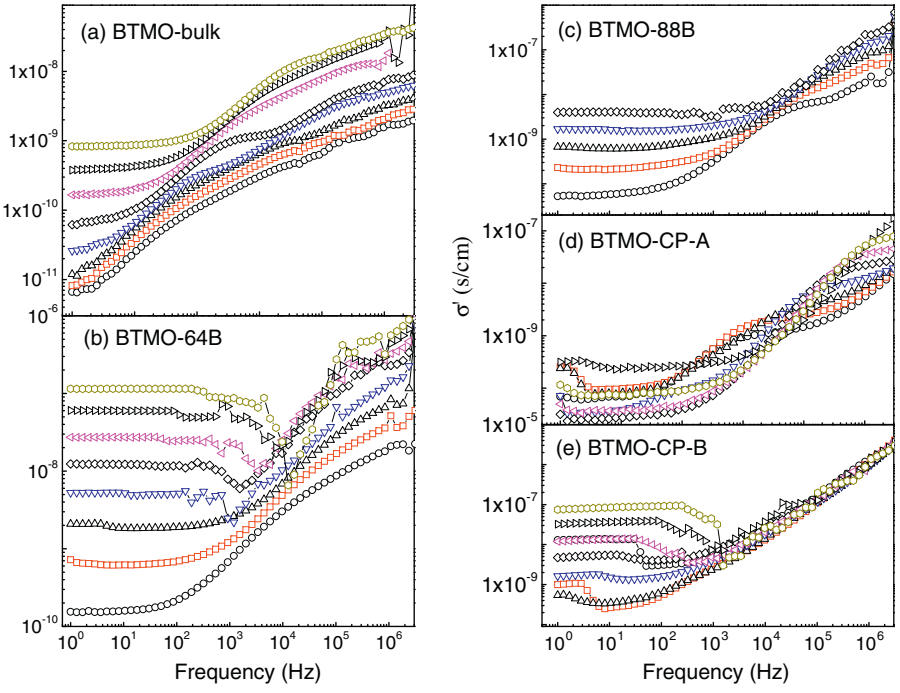

Fig. 3. Log–log plot of the variation of $\sigma'(f)$ at selected temperatures for different samples.

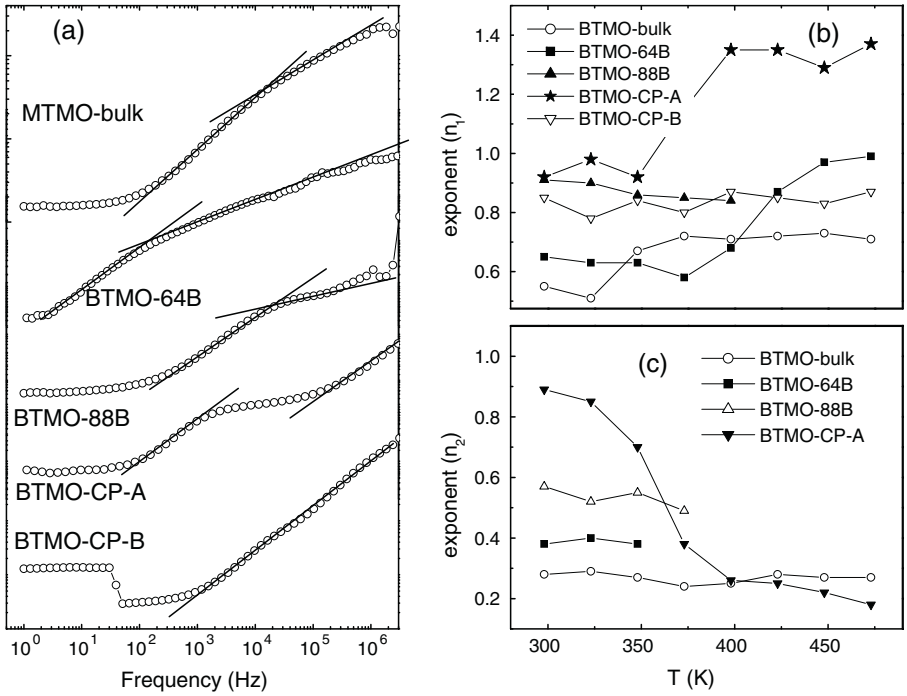

Fig. 4. (a) Log–log plot of the variation of $\sigma'(f)$ at 298 K for different samples. The lines guide to the linear fit of the experimental data. The exponents (n_1 and n_2) are shown in (b) and (c) respectively.

298–473 K for BTMO-bulk (Fig. 3(a)), BTMO-64B (Fig. 3(b)), BTMO-88B (Fig. 3(c)), BTMO-CP-A (Fig. 3(d)), and BTMO-CP-B (Fig. 3(e)) samples. BTMO samples showed nearly a frequency independent conductivity at lower frequencies. The highly insulating nature (low conductivity $\sim 10^{-11}$–10^{-8} S/cm) and constant conductivity over a wide range of lower frequencies in some of the samples (BTMO-64B, BTMO-88B, BTMO-CP-B) are useful for designing good quality resistors. Interestingly, BTMO-64B (Fig. 3(b)) and BTMO-CP-B (Fig. 3(e)) showed a conductivity minimum in between the frequency independent and frequency dependent conductivity regimes. This minimum becomes prominent at higher measurement temperatures. In the frequency dependent regime, ac conductivity ($\sigma'(f)$) of BTMO obeys Jonscher's power law [29]: $\sigma'(f) \sim f^n$; f is applied frequency, n is exponent. We have noted two exponents; one (n_1) at lower frequency regime and second one (n_2) is at higher frequency regime. The conductivity at higher frequency regime is slowing down (with lower exponent n_2) in comparison with lower frequency activated regime (with higher exponent n_1). In the absence of free charge carriers in ceramic materials, such slowing down of ac conductivity arises due to unsuccessful attempts of the bound charge carriers (polarons) to follow the driving electric field at higher frequencies [30,31]. Fig. 4(a) shows the fit of room temperature $\sigma'(f)$ data with two exponents (n_1 and n_2). Single exponent is applicable only for BTMO-CP-B sample. The n_1 values (Fig. 4(b)) are in the range 0.95–0.50 for all samples, except $n_1 \sim 1.1$–1.4 in BTMO-CP-A sample above 350 K. The exponent value is generally less than 1, but exponent value greater than 1 indicates a distribution of conduction paths for charge motion [32]. The n_2 value in most of the BTMO samples lies in the range 0.6–0.2. BTMO-CP-A sample showed n_2 value above 0.6 at temperature below 350 K. The Jonscher power law exponent (n) in many ferroelectric perovskite oxides has shown the value nearly 1 and the lower values of n are attributed to the heterogeneous microstructure [33]. The exponent n_1 (>0.5) suggests short-ranged single polaron hopping at inhomogeneous electronic microstructure of grain boundaries, whereas smaller value of $n_2 < 0.5$ suggests the multi-polaron hopping mostly in the conducting grains or at the inhomogeneous interfaces of grains and grain boundaries [30,33].

3.2.2. Electrical impedance

We calculate the resistivity contribution from grains and grain boundaries using Cole–Cole plot (imaginary part ($-Z''$) vs. real part (Z')) of complex impedance spectrum. Intercept of the semicircle on higher side of Z' axis gives the estimation of grain boundary resistance (R_{gb}), and also corresponding grain boundary resistivity (ρ_{gb}) by incorporating the dimension of the sample. Fig. 5(a) shows the Cole–Cole plot for BTMO-bulk sample at selected temperatures, where lines indicate the fit curves of the impedance data to semi-circles. Fig. 5(b) shows the single semi-circle to the complex impedance data at 298 K for different samples. Center of these circles located below Z' axis. This indicates non-Debye type dielectric relaxation in the samples and affected by the heterogeneous microstructure [33]. Electrode effect (impedance data nearly parallel to $-Z''$ axis) is prominent only in mixed phased BTMO-64MA sample. Electrode effect is not significant in other samples. However, impedance data of BTMO-CP-A sample (Fig. 5(c)) are fitted with two semi-circles. Semi-circle at lower Z' value gives the resistance of grains (R_g) and semi-circle at higher Z' value gives R_{gb}. The analysis shows the room temperature grain boundary resistivity (ρ_{gb}) of BTMO samples ~2662, 60, 196, 162 and 36

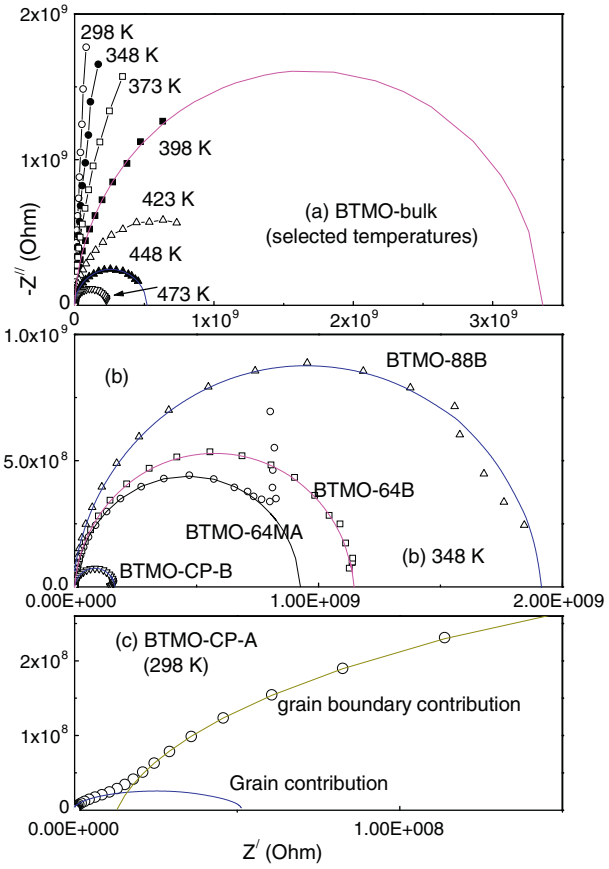

Fig. 5. Cole–Cole plot of complex impedance $(-Z'', Z')$ for different samples at selected temperatures. Color lines show the fit of data to semi-circle.

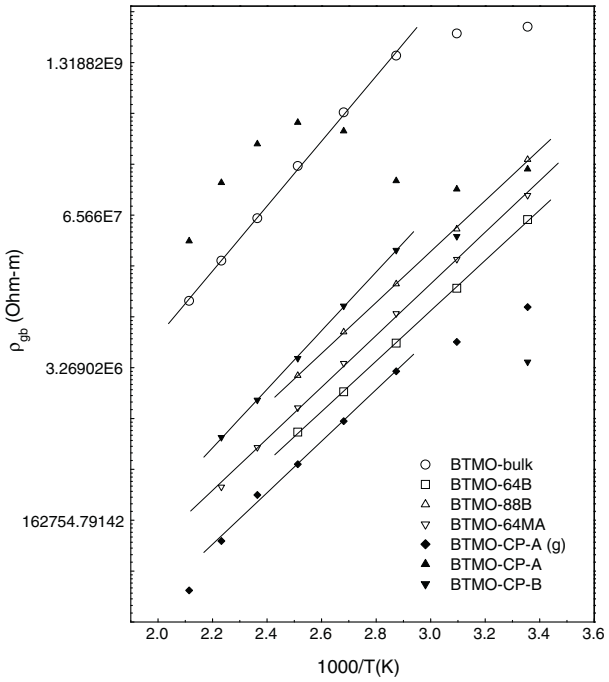

Fig. 6. Grain boundary resistivity (ρ_{gb}) vs. 1000/T plot for different samples. Solid lines show the fit of data to Arrhenius law. Grain resistivity (ρ_g) of BTMO-CP-A sample is also shown in the plot.

in M Ω-m unit for BTMO-bulk, BTMO-64B, BTMO-88B, BTMO-CP-A and BTMO-CP-B samples, respectively. The order of ρ_{gb} (at 298 K) suggests that the samples belong to the class of semiconductor/insulator.

Fig. 6 shows the temperature dependence of resistivity (ρ_g, ρ_{gb} in log scale) to verify the thermal activated conductivity mechanism according to Arrhenius law: $\rho(T) = \rho_0 \exp[-E_a/K_BT]$. Here, E_a is the activation energy, K_B is the Boltzmann's constant, ρ_0 is the prefactor. It may be noted that there is a signature of PTCR (positive temperature coefficient of resistance) at lower temperature ρ_{gb} (T) data, particularly for chemical routed (BTMO-CP-A and BTMO-CP-B) samples, and similar to the feature of $BaTiO_3$ ceramics [34,35]. All the samples have shown negative temperature coefficient of resistance (NTCR) at higher temperatures. It may be noted that grain boundary conductivity of the mechanical alloyed samples is lower in comparison with solid state sintering and chemical routed samples. The activation energy (E_a) was calculated from the linear slope (straight line in Fig. 6) of the NTCR region of the ρ_{gb} (T) data. Table 2 shows the obtained values of E_a. E_a was not calculated for BTMO-CP-A sample due to limited NTCR region of ρ_{gb} (T) below 473 K. However, E_a has been calculated from ρ_g (T) data of BTMO-CP-A sample. The calculated values of E_a (0.26–0.55 eV) are in good agreement with earlier reports [15,36]. The range of activation energy suggests different types of hopping mechanism across the grain boundaries of the samples, which are heterogeneous in nature [33].

3.2.3. Dielectric constant

Fig. 7 shows the frequency dependent real (ε') and imaginary (ε'') parts of dielectric constant (ε) for BTMO-bulk sample. As shown for BTMO-bulk, the dielectric constant (ε) of BTMO samples are also controlled by ε' and ε'' at higher and lower frequency regime (below 10–100 Hz), respectively. A strong increase of ε'' (also ε) at low frequency regime is attributed to interfacial polarization of the grains [9,15]. The magnitude of ε' slowly decreases with the increase of frequency before leveling off to a constant value at higher frequencies. This is a commonly observed feature in ceramic materials. Such decrease of dielectric constant in $BaTiO_3$ based ceramics is attributed to the fact that some of the soft phonon modes in distorted Ti–O_6 bonds do not follow the ac field at higher frequencies [37,38]. Fig. 8(a–d) shows the frequency dependent ε of BTMO-64B, BTMO-88B, BTMO-CP-A and BTMO-CP-B samples. The dielectric properties of BTMO-CP-A sample are drastically different from other samples. The dielectric constant of BTMO-CP-A sample is relatively small and two steps behavior is exhibited in the frequency scale. Two steps behavior indicates typical heterogeneous electrical structure in chemical routed sample, particularly at lower annealing temperature. Similar feature in Yb modified $CaTiO_3$ perovskite was interpreted in terms of Maxwell–Wagner interfacial effect [39]. The large dielectric constant at lower frequencies of BTMO samples is comparable to the values in many advanced ferroelectric materials [31,38–40]. We understand that the huge dielectric constant (10^3–10^6) may not be the intrinsic property,

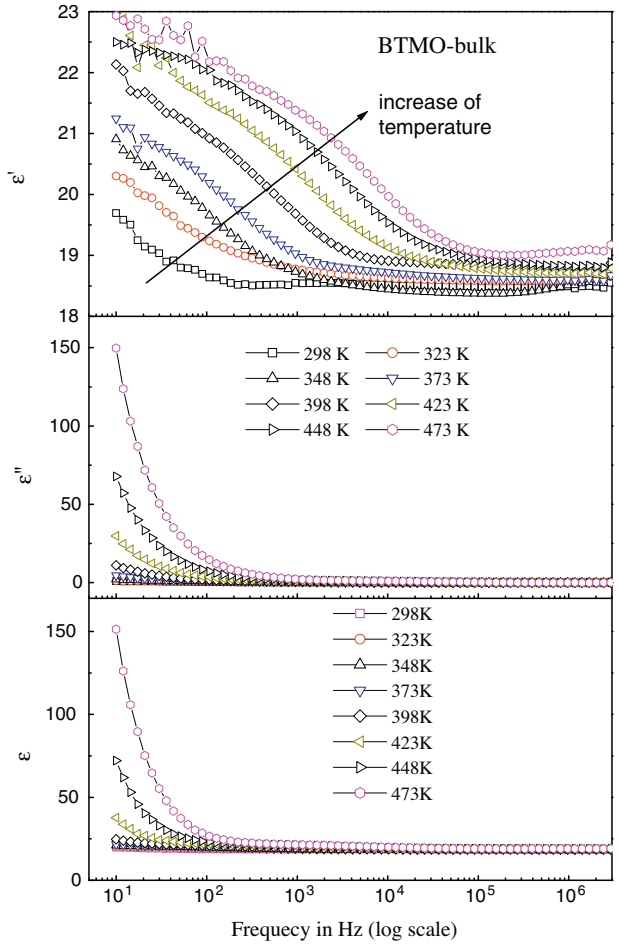

Fig. 7. Frequency dependent dielectric constant (real: ε', imaginary: ε'' and resultant: ε) at different temperatures for BTMO-bulk sample.

i.e., contribution of dipolar orientation alone [13]. In order to confirm the interfacial effect on dielectric parameters, Cole–Cole plot was used to estimate the intrinsic values of the dielectric constant. Some plots are shown in Fig. 9(a–c) for 298 K data. The Cole–Cole plot of complex dielectric constant (ε'' vs. ε') shows interfacial contribution (steep increase of ε'' in ε'' vs. ε' plot) in all samples at lower frequencies, i.e., at higher values of ε'. We have taken lower intercepted value of the semi-circle on ε' axis as the contribution of ε from grains (ε_g) and higher intercepted value as the contribution of ε from grain boundaries (ε_{gb}). The contributions from grains and grain boundaries are separately seen from two semi-circles in BTMO-CP-A and BTMO-CP-B samples (Fig. 9(c)). Most important information from Cole-to-Cole plot is that intrinsic values of the dielectric constant in BTMO samples lie in the range 4–30, although ε value up to 10^3–10^6 was noted in Figs. 7 and 8. The grain boundary contribution (ε_{gb}) of BTMO-CP-B sample has notably increased up to 355 at 398 K. This chemical routed sample, which is annealed at higher temperature, gives the better signature of ferroelectric properties. One distinct feature from the SEM picture is that surface compactness/connectivity of the particles in BTMO-CP-B sample is very good. We understand that surface compactness of the particles is playing an important role in determining the intrinsic values of dielectric constant in ceramics [14]. The decreased dielectric constant of BTMO samples in comparison with the reported dielectric constant (200–7000) of BTO sample could be associated to the increased disorder in less symmetric crystal structure. This in turn reduces the dielectric polarization of the Mn doped $BaTiO_3$ system.

3.2.4. Electrical modulus

The main advantage of applying modulus formalism is to suppress the electrode effect on electric conductivity contribution. BTMO-bulk sample (Fig. 10) shows a sharp increase of M′below 100 Hz, followed by a slow increase with frequencies and finally, saturated above 100 kHz. The imaginary part of modulus (M'') shows a sharp peak at lower frequency (below 100 Hz) and the peak position shifts to higher frequencies with the increase of measurement temperature. In conductive relaxation process the real part of modulus (M') generally exhibits a sharp monotonic increase with frequencies where as the imaginary part of the electric modulus (M'') shows a peak at lower frequencies (below 100 Hz). Based on the observation of a gradual increase of M' at low frequency regime, along with broad peak in M'', we conclude that the dielectric response of BTMO-bulk sample (also other BTMO samples) is non-conductive type and the dynamics is affected by Maxwell–Wagner interfacial relaxation [33,39]. The shape of the resultant electrical modulus (M) in BTMO-bulk sample (also in all samples) is determined mainly by M' and M'' does not have significant effect. As shown in Fig. 11(a–d), other BTMO samples, irrespective of the synthesis routes, have exhibited Maxwell–Wagner type interfacial relaxation peak at relatively higher frequencies. The shifting of the relaxation peak to higher frequencies with increasing measurement temperature shows a typical short range hopping of charge carriers/polarons between conducting ions (Mn^{4+}, Mn^{2+}, Ti^{3+}, Ti^{4+}) [21]. The exceptional case is noted only for chemical routed BTMO-CP-A and BTMO-CP-B samples that showed two contributions in relaxation mechanism. Such dielectric property indicates a heterogeneous micro-structure at the grain and grain-boundary interfaces [31,33,39]. For BTMO-CP-A sample (Fig. 11(c)), the low frequency peak represents the range of frequency at which the conducting charge carriers (polarons) reflect long range hopping whereas at high-frequency side the carriers are spatially confined to their potential well and exhibit a short range hopping [29]. For BTMO-CP-B sample (Fig. 11(d)), there is a multiple contribution to short range hopping at higher frequency side and indicates more heterogeneity at the local electronic structure. In fact, Cole–Cole plots of the electrical modulus (M'' vs. M') for the chemical routed samples in Fig. 12(a and b) have revealed two semi-circles (relaxation peaks). The peak at higher values of M' (higher frequency side) corresponds to the capacitance from grains and the peak at lower values of M' (lower frequency side) corresponds to the capacitance from grain boundaries. For chemical routed samples, the dielectric relaxation from grains is comparable to that from the grain boundaries. However, two peaks relaxation feature of the chemical routed samples is different

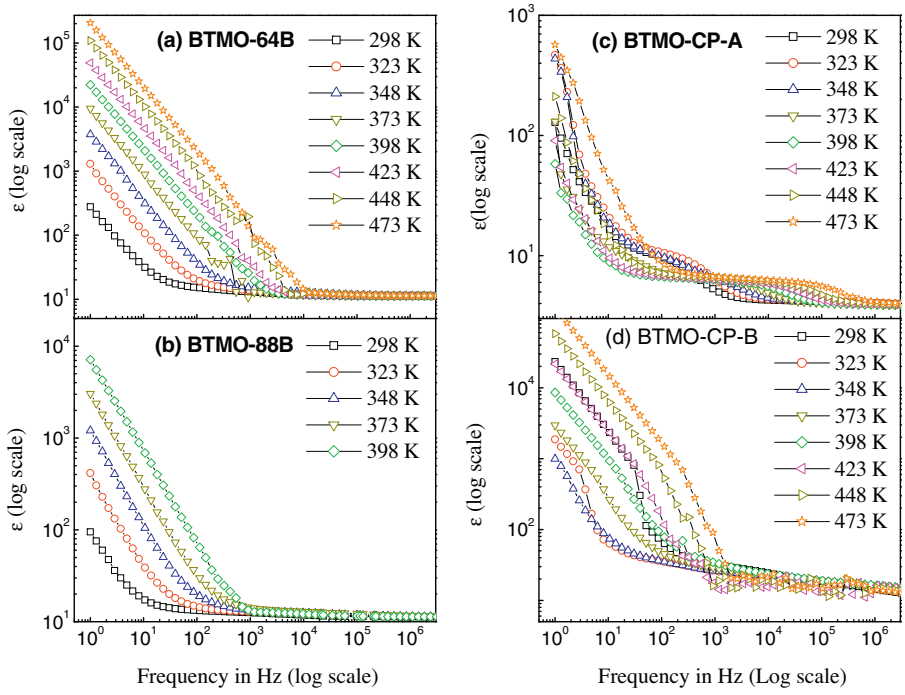

Fig. 8. Frequency dependent dielectric constant (ε) at different temperatures for BTMO-64B (a), BTMO-88B (b), BTMO-CP-A (c), and BTMO-CP-B (d) samples.

from the structurally heterogeneous (multi-phased) BTMO-64MA sample (Fig. 12(c)). In BTMO-bulk (Fig. 12(d)) and mechanical alloyed samples (data not shown), the dielectric relaxation (major peak) from grain boundaries is dominating over the grains (minor peak). These two peaks feature of the solid state and mechanical alloyed samples in complex modulus plot is different from the single peak in complex impedance plot (Fig. 9). This is due to the fact that imaginary part of the impedance (Z'') manifests the largest resistance of the sample, where contribution of the low resistive grains may not be properly reflected. On the other hand, the imaginary part of the electrical modulus (M'') responds to the smallest capacitance,

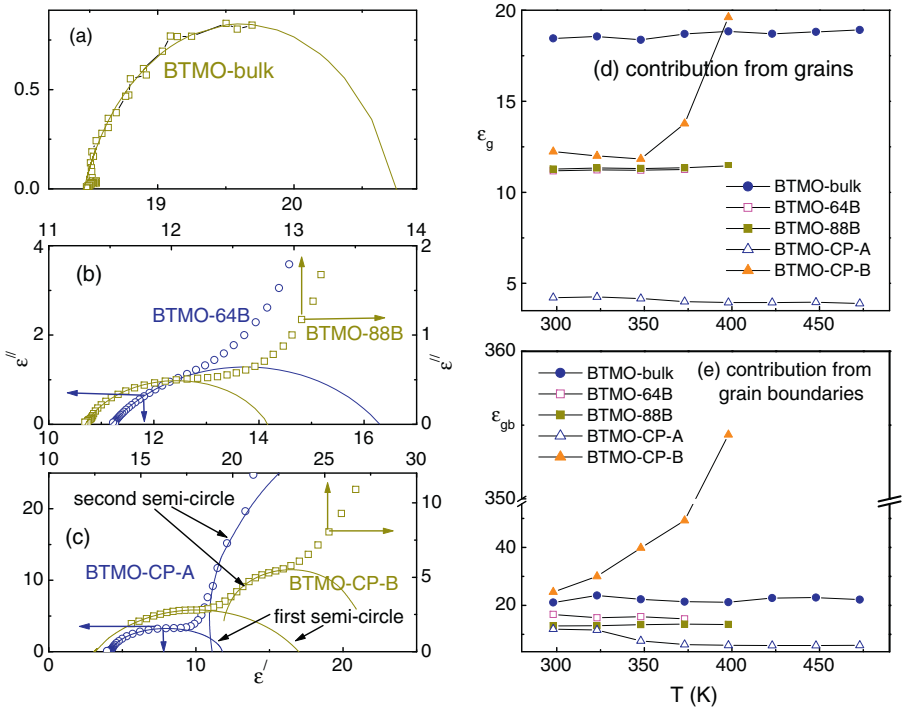

Fig. 9. Cole–Cole plot (ε'' vs. ε') of different samples at 298 K. Solid lines show the fit data. The dielectric constant from grain and grain-boundary contributions are shown in (d) and in (e) respectively.

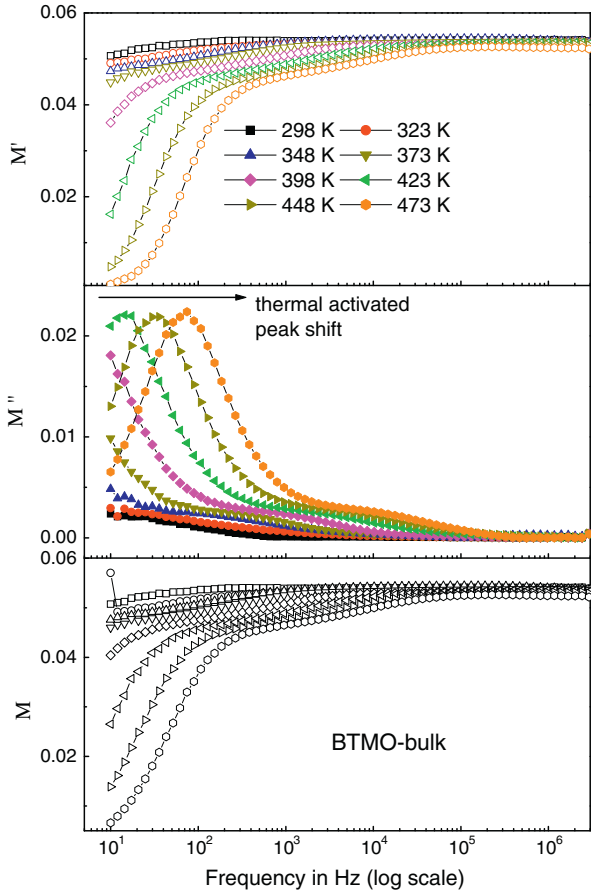

Fig. 10. Frequency dependent modulus at different temperatures for BTMO-bulk samples.

i.e., highly conductive part, of the sample [33]. We conclude that the interfacial/grain boundary electronic structure has been drastically modulated in chemical routed samples in comparison with mechanical and solid state routed samples. Applying the condition of $2\pi\tau f_m = 1$ at peak position of $M''(f)$ in Cole–Cole plot, we have calculated relaxation time τ_g and τ_{gb} at different temperatures for grains and grain boundaries, respectively. The relaxation time (τ) was used in Arrhenius law: $\tau_{g,\,gb}(T) = \tau_{g0,\,gb0} \exp(E_a/K_BT)$ to check the activation energy (E_a) and characteristic relaxation time ($\tau_{g0,\,gb0}$) (values are shown in Table 2). It may be noted that activation energy from relaxation time is well matched to the values from impedance data and $\tau_{g0,\,gb0}$ values are comparable to the reports of ferroelectric perovskite system [33]. The characteristic relaxation time (τ_{gb0}) from grain boundaries of the chemical routed samples is significantly large in comparison with other samples.

3.2.5. Dielectric loss

The dielectric loss (tan δ) is an important parameter that determines the suitability of a dielectric material in microelectronic devices. Fig. 13(a–e) shows the variation of dielectric loss with frequencies at selected measurement temperatures. The common feature is that dielectric loss decreases with the increase of frequency. Some of the samples, e.g., BTMO-CP-A sample (Fig. 13(d)), have shown thermal activated sharp loss peak. The peak position of BTMO-CP-A sample shifts to higher frequencies (f_m) with the increase of measurement temperature (T). This follows Arrhenius law: $f_m(T) = f_0 \exp(-E_a/K_BT)$ with activation energy (E_a) = 0.45 eV and attempt frequency (f_0) = 9.74×10^9 Hz. Dielectric loss in BTMO samples is reasonably low, e.g., 10–10^{-4} for BTMO-bulk, 6000–10^{-2} for BTMO-64B, 10^2–10^{-2} for BTMO-88B, 10–10^{-2} for BTMO-64-A and 10–0.1 for BTMO-CP-B samples, respectively. The high dielectric loss at lower frequencies in some of the BTMO samples is the effect of interfacial loss, but dielectric loss is below 0.1 at higher frequencies (i.e., in radio frequencies and above) for all BTMO samples.

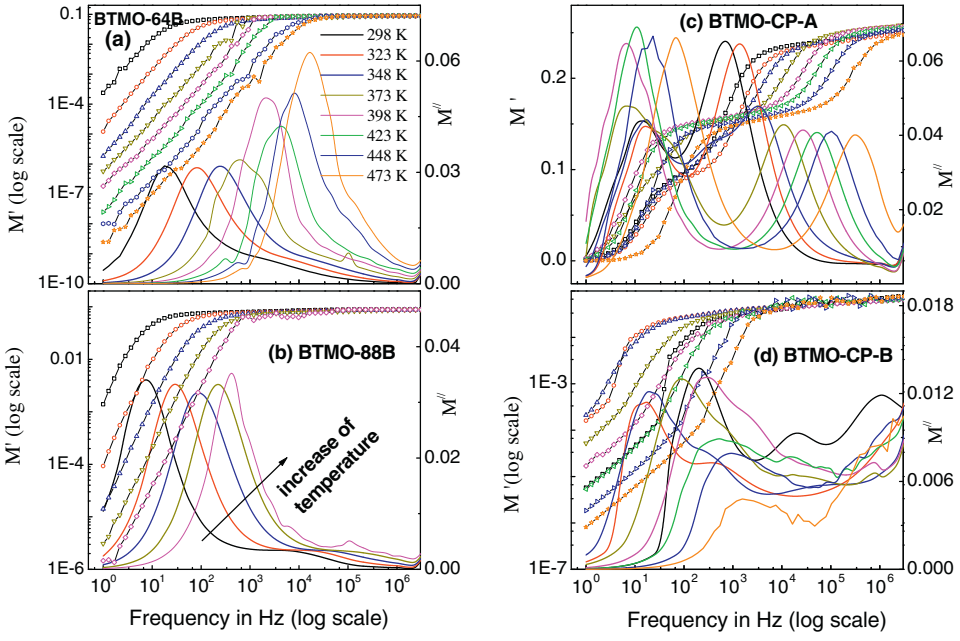

Fig. 11. Frequency dependent electrical modulus (real: M' and imaginary: M'' components) of selected samples at different temperatures.

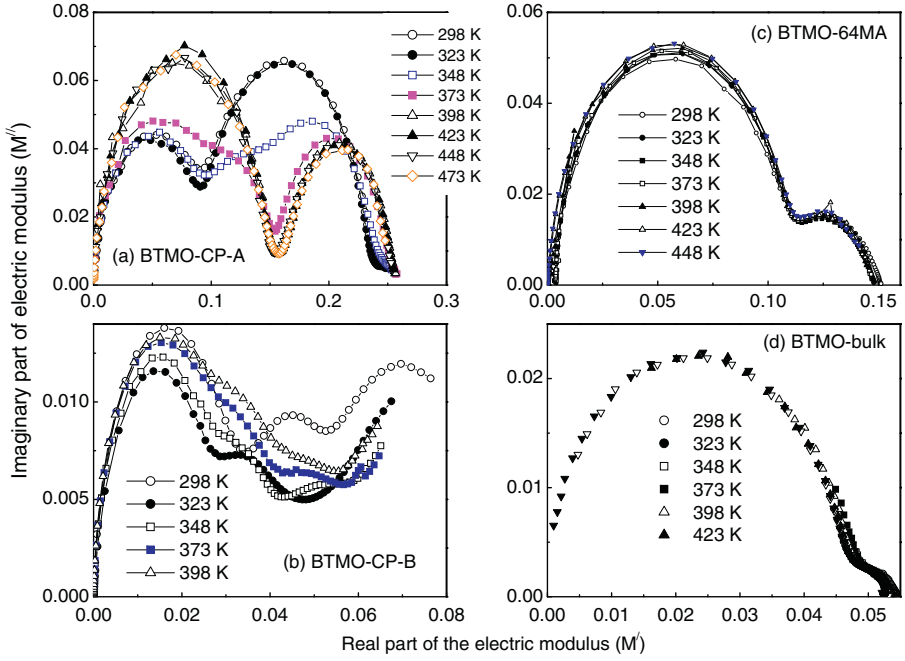

Fig. 12. Cole–Cole plot for the M'' vs. M' data at selected temperatures for selected samples.

3.3. Magnetic properties

We have recorded magnetic field dependent dc magnetization (Fig. 14) for verifying the at room temperature ferromagnetism, as indicated in some of the recent works of magnetic atom doped $BaTiO_3$ samples [18,37,41,42]. BTMO-bulk sample (Fig. 14(a) shows typical paramagnetic character at room temperature. The paramagnetic contribution dominates in the $M(H)$ data within the field range −15 K to +15 K and magnetic moment at 15 kOe is nearly 0.115 emu/g for all BTMO samples, irrespective of the synthesis routes. However, there is ferromagnetic signature (small hysteresis loop width in the low field regime) in some of the BTMO samples. The insets of Fig. 14(d–e) clearly show the ferromagnetic signature in chemical routed samples. Defect structure and phase separation have shown remarkably large ferromagnetism in BTMO [40] and in $BaTiO_3$ nanoparticles [22]. Considering weak signature of room temperature ferromagnetism in our BTMO samples,

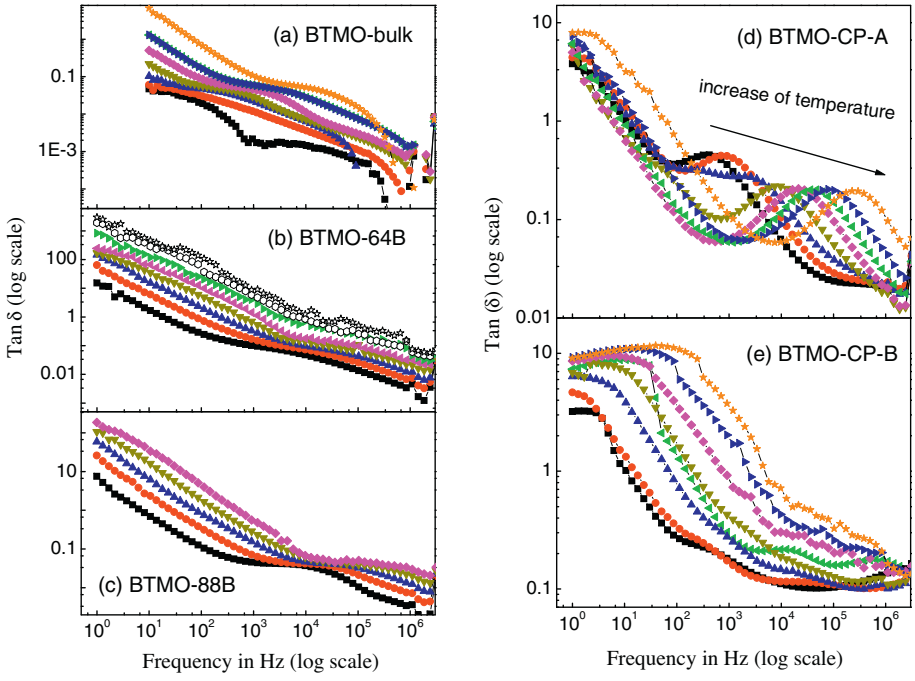

Fig. 13. Frequency dependent dielectric loss for different samples at selected temperatures.

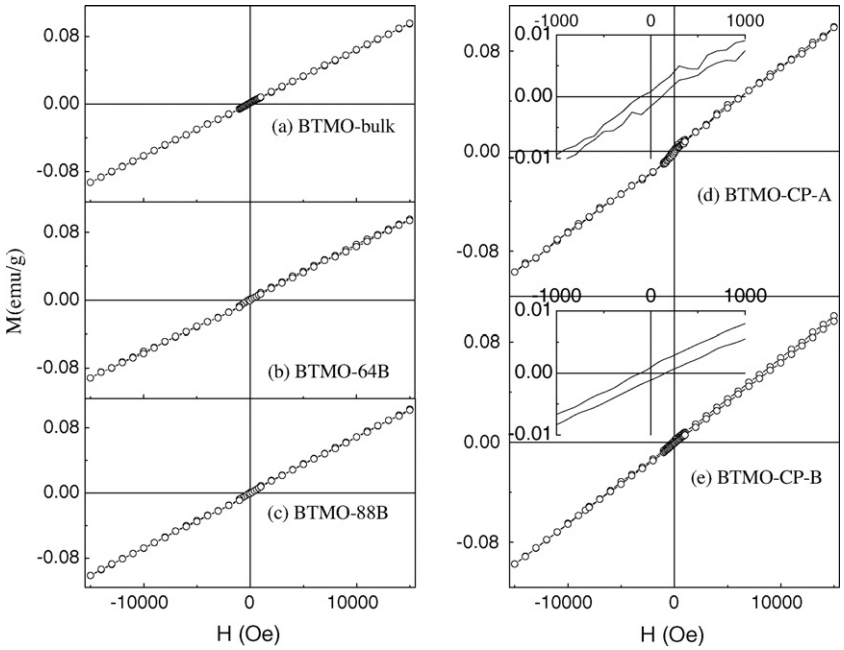

Fig. 14. Field dependent dc magnetization at room temperature for different samples. Insets show the possible loop (y axis: M(emu/g)) at lower fields.

we understand that ferromagnetic signature may not due to defective structure. This could be attributed to the effect of magnetic Mn doping in $BaTiO_3$ ceramics [22].

4. Conclusions

Present work shows that interfacial electronic microstructure of the grains and grain boundaries in chemical routed samples is significantly different in comparison with mechanical and solid state routed samples. This is attributed to the smaller grain size of the chemical routed samples. Dielectric relaxation from grains and grain boundaries are competitive in chemical routed samples, where as grain boundaries are dominating over grains in other samples. Chemical routed samples showed better signature of room temperature ferromagnetism, relatively large dielectric constant, two steps dielectric relaxation and low dielectric loss at high frequencies. The interfacial effects caused huge dielectric constant at lower frequencies in all BTMO samples, but their intrinsic dielectric constant, except chemical routed sample at higher annealing temperature, lies in the range 4–30. The enhancement of dielectric constant in chemical routed sample is assisted by the better connectivity of the particles (semi-melt like state) and Maxwell–Wagner type interfacial polarization that has been engineered by changing the route of material synthesis. The significant aspect of this work is that interfacial polarization can be controlled at relatively low annealing temperature (1273–1423 K) in chemical and mechanical alloyed samples in comparison with the high sintering temperature (1473 K) of solid state routed ceramic sample. Hence, chemical and mechanical alloyed routes could be useful for designing application-oriented ceramics.

Acknowledgments

Author thanks to Mr. K. Samuvel for being associated in experimental work. Author also thanks to CIF, Pondicherry University for providing experimental facilities.

References

[1] M. Fiebig, N.A. Spaldin, Current trends of the magnetoelectric effect, Eur. Phys. J. B 71 (2009) 293–297.
[2] M. Liu, O. Obi, J. Lou, Y. Chen, Z. Cai, S. Stoute, M. Espanol, M. Lew, X. Situ, K.S. Ziemer, V.G. Harris, N.X. Sun, Giant electric field tuning of magnetic properties in multiferroic ferrite/ferroelectric heterostructures, Adv. Funct. Mater. 19 (2009) 1826–1831.
[3] A.N. Ulyanov, D.S. Yang, A.S. Mazur, V.N. Krivoruchko, G.G. Levchenko, I.A. Danilenko, T.E. Konstantinova, Local structure and magnetic inhomogeneity of nano-sized $La_{0.7}Sr_{0.3}MnO_3$ manganites, J. App. Phys. 109 (2011) 123928.
[4] P.K. Siwach, H.K. Singh, O.N. Srivastava, Low field magnetotransport in manganites, J. Phys.: Condens. Matter 20 (2008) 273201–273244.
[5] W. Kleemann, S. Bedanta, P. Borisov, V.V. Shvartsman, S. Miga, J. Dec, A. Tkach, P.M. Vilarinho, Multiglass order and magnetoelectricity in Mn^{2+} doped incipient ferroelectrics, Eur. Phys. J. B 71 (2009) 407–410.
[6] Yi Zhang, J. Liu, X.H. Xiao, T.C. Peng, C.Z. Jiang, Y.H. Lin, C.W. Nan, Large reversible electric–voltage manipulation of magnetism in NiFe/$BaTiO_3$ heterostructures at room temperature, J. Phys. D: Appl. Phys. 43 (2010) 082002.
[7] D. Chiba, M. Yamanouchi, F. Matsukura, H. Ohno, Electrical manipulation of magnetization reversal in a ferromagnetic semiconductor, Science 301 (2003) 943–945.
[8] Y.-H. Chu, L.W. Martin, M.B. Holcomb, M. Gajek, S.J. Han, Q. He, N. Balke, C.H. Yang, D. Lee, W. Hu, Q. Zhan, P.L. Yang, A. Fraile-Rodriguez, A. Scholl, S.X. Wang, R. Ramesh, Electric-field control of local ferromagnetism using a magnetoelectric multiferroic, Nat. Mater. 7 (2008) 478–482.
[9] N. Izyumskaya, Ya Alivov, H. Morkoç, Oxides, and more oxides: high-κ oxides, ferroelectrics, ferromagnetics, and multiferroics, Crit. Rev. Solid State Mater. Sci. 34 (2009) 89–179.

[10] W. Maison, R. Kleeberg, R.B. Heimann, S. Phanichphant, Phase content, tetragonality, and domain size of nanoscaled barium titanate sythesized by the catecholate process: effect of calcination temperature, J. Eur. Ceram. Soc. 23 (2003) 127–132.
[11] G. Arlt, D. Hennings, G. de With, Dielectric properties of fine-grained barium titanate ceramics, J. Appl. Phys. 58 (1985) 1619.
[12] L. Wu, M. Chure, K. Wu, W. Chang, M. Yang, W. Liu, M. Wu, Dielectric properties of barium titanate ceramics with different materials powder size, Ceram. Int. 35 (2009) 957–960.
[13] T. Hoshina, K. Takizawa, J. Li, T. Kasama, H. Kakemoto, T. Tsurumi, Domain size effect on dielectric properties of barium titanate ceramics, Jpn. J. Appl. Phys. 47 (2008) 7607–7611.
[14] Y. Zou, Y. Wu, X. Guo, S. Tong, Z. Wang, L. Zhang, Effect of particle size on the densification and dielectric properties of $BaTiO_3$ ceramics prepared by liquid phase sintering, Phys. Status Solidi A 209 (2012) 243–247.
[15] M.T. Busacglia, V. Busaglia, M. Viviani, J. Petzelt, M. Savinov, L. Mitoseriu, A. Testino, P. Nanni, C. Harnagea, Z. Zhao, M. Nygren, Ferroelectric properties of dense nanocrystalline $BaTiO_3$ ceramics, Nanotechnology 15 (2004) 1113–1117.
[16] S. Wada, T. Hoshina, H. Yasuno, M. Ohishi, H. Kakemoto, T. Tsurumi, M. Yashima, Size effect of dielectric properties for barium titanate particles and its model, Key Eng. Mater. 301 (2006) 27–30.
[17] K.F. Wang, J.-M. Liu, Z.F. Ren, Multiferroicity: the coupling between magnetic and polarization orders, Adv. Phys. 58 (2009) 321–448.
[18] H. Nakayama, H. Katayama-Yoshida, Theoretical prediction of magnetic properties of $Ba(Ti_{1-x}M_x)O_3$ (M = Sc, V, Cr, Mn, Fe, Co, Ni, Cu), Jpn. J. Appl. Phys. 40 (2001) L1355–L1358.
[19] T. Li, L. Li, J. Zhao, Z. Gui, Modulation effect of Mn^{2+} on dielectric properties of $BaTiO_3$-based X7R materials, Mater. Lett. 44 (2000) 1–5.
[20] Y. Takezawa, K. Kobayashi, F. Nakasone, T. Suzuki, Y. Mizuno, H. Imai, Mn-doped $BaTiO_3$ thin film sintered using nanocrystals and its dielectric properties, Jpn. J. Appl. Phys. 48 (2009) 111408.
[21] Y. Shuai, S. Zhou, H. Schmidt, Electrical and magnetic properties of polycrystalline Mn-doped $BaTiO_3$ thin films grown on Pt/sapphire substrates by pulsed laser deposition, Adv. Sci. Tech. 67 (2010) 212–217.
[22] S. Qin, D. Liu, Z. Zuo, Y. Sang, X. Zhang, F. Zheng, H. Liu, X. Xu, UV-irradiation-enhanced ferromagnetism in $BaTiO_3$, J. Phys. Chem. Lett. 1 (2010) 238–241.
[23] L. Miranda, A. Feteira, D.C. Sinclair, K. Boulahya, M. Hernando, J. Ramírez, A. Varela, J.M. González-Calbet, M. Parras, Composition–structure–property relationships of 6H- and 12R-type hexagonal $Ba(Mn,Ti)O_{3-\delta}$ Perovskites, Chem. Mater. 21 (2009) 1731–1742.
[24] S. Ohara, A. Kondo, H. Shimoda, K. Sato, H. Abe, M. Naito, Rapid mechanochemical synthesis of fine barium titanate nanoparticles, Mater. Lett. 62 (2008) 2957–2959.
[25] L.B. Konga, J. Maa, H. Huanga, R.F. Zhanga, W.X. Que, Barium titanate derived from mechanochemically activated powders, J. Alloys Compd. 337 (2002) 226–230.
[26] C.G. Hu, H. Liu, C.S. Lao, L.Y. Zhang, D. Davidovic, Z.L. Wang, Size-manipulable synthesis of single-crystalline $BaMnO_3$ and $BaTi_{1/2}Mn_{1/2}O_3$ nanorods/nanowires, J. Phys. Chem. B 110 (2006) 14050–14054.
[27] R. Yimnirun, J. Tangsritrakul, S. Rujirawat, S. Limpijumnong, Identification of Mn site in $BaTiO_3$ by synchrotron X-ray absorption spectroscopy measurements, Ferroelectrics 381 (2009) 130–243.
[28] Yu-Chuan Wu, Sea-Fue Wang, Shin-Hong Chen, Microstructural investigation of $Ba(Ti(1\_x)Mn_x)O_3$ ceramics with 6H- and 12R-polytypes, J. Am. Ceram. Soc. 92 (2009) 2099–2108.
[29] A. Shukla, R.N.P. Choudhary, A.K. Thakur, Thermal, structural and complex impedance analysis of Mn^{4+} modified $BaTiO_3$ electroceramic, J. Phys. Chem. Solids 70 (2009) 1401–1407.
[30] I. Panneer Muthuselvam, R.N. Bhowmik, Connectivity between electrical conduction and thermally activated grain size evolution in Ho-doped $CoFe_2O_4$ ferrite, J. Phys. D: Appl. Phys. 43 (2010) 465002.
[31] M. Idrees, M. Nadeem, M. Mehmood, M. Atif, K.H. Chae, M.M. Hassan, Impedance spectroscopic investigation of delocalization effects of disorder induced by Ni doping in LaFeO3, J. Phys. D: Appl. Phys. 44 (2011) 105401.
[32] A.N. Papathanassiou, I. Sakellis, J. Grammatikakis, Universal frequency-dependent ac conductivity of conducting polymer networks, Appl. Phys. Lett. 91 (2007) 122911.
[33] R. Martínez, A. Kumar, R. Palai, J.F. Scott, R.S. Katiyar, Impedance spectroscopy analysis of $Ba_{0.7}Sr_{0.3}TiO_3/La_{0.7}Sr_{0.3}MnO_3$ heterostructure, J. Phys. D: Appl. Phys. 44 (2011) 105302.
[34] C. Gillot, J.-Pierre Michenaud, I. Baukens, P.-Henri Duvigneaud, Microscopic origin of the PTC effect in niobium-doped barium titanate, J. Am. Ceram. Soc. 80 (1997) 1043–1046.
[35] O.I. V'yunov, L.L. Kovalenko, A.G. Belous, The effect of isovalent substitutions and dopants of 3d-metals on the properties of ferroelectrics semiconductors, Condens. Matter Phys. 6 (2003) 213–220.
[36] C.-Gang Duan, R.F. Sabirianov, W.-Ning Mei, S.S. Jaswal, E.Y. Tsymbal, Interface effect on ferroelectricity at the nanoscale, Nano Lett. 6 (2006) 483–487.
[37] V. Petkov, V. Buscaglia, M.T. Buscaglia, Z. Zhao, Y. Ren, Structural coherence and ferroelectricity decay in submicron- and nano-sized perovskites, Phys. Rev. B 78 (2008) 054107.
[38] H. Zhang, X. Deng, T. Li, W. Zhang, R. Chen, W. Tian, J. Li, X. Wang, L. Li, Extrinsic effects on dielectric response of ultrafine grain $BaTiO_3$ ceramics, Appl. Phys. Lett. 97 (2010) 162913.
[39] M. Viviani, M. Bassoli, V. Buscaglia, M.T. Buscaglia, P. Nanni, Giant permittivity and Maxwell–Wagner relaxation in Yb: $CaTiO_3$ ceramics, Phys. D: Appl. Phys. 42 (2009) 175407.
[40] Md G. Masud, B.K. Chaudhuri, H.D. Yang, High dielectric permittivity and room temperature magneto-dielectric response of charge disproportionate $La_{0.5}Ba_{0.5}FeO_3$ perovskite, J. Phys. D: Appl. Phys. 44 (2011) 255403.
[41] X. Tong, Yuan-Hua Lin, S. Zhang, Y. Wang, Ce-Wen Nan, Preparation of Mn-doped $BaTiO_3$ nanoparticles and their magnetic properties, J. Appl. Phys. 104 (2008) 066108.
[42] B. Xu, K.B. Yin, J. Lin, Y.D. Xia, X.G. Wan, J. Yin, X.J. Bai, J. Du, Z.G. Liu, Room-temperature ferromagnetism and ferroelectricity in Fe-doped $BaTiO_3$, Phys. Rev. B 79 (2009) 134109.